

Harnessing Distributed Acoustic Sensing for Earthquake Early Warning: Magnitude Estimation and Ground Motion Prediction

Itzhak Lior^{1*}, Diane Rivet², Jean-Paul Ampuero², Anthony Sladen², Sergio Barrientos³, Rodrigo Sánchez-Olavarria³, German Alberto Villarroel Opazo⁴, Jose Antonio Bustamente Prado⁴

¹Institute of Earth Sciences, The Hebrew University, Jerusalem, Israel

²Université Côte d'Azur, CNRS, Observatoire de la Côte d'Azur, IRD, Géoazur, France

³Centro Sismológico Nacional, Universidad de Chile, Santiago, Chile

⁴Gtd Grupo S.A., Santiago, Chile

Corresponding author: Itzhak Lior (itzhak.lior@mail.huji.ac.il)

This is a non-peer reviewed pre-print submitted to EarthArXiv

Abstract

Earthquake Early Warning (EEW) systems provide seconds to tens of seconds of warning time before potentially-damaging ground motions are felt. For optimal warning times, seismic sensors should be installed as close as possible to expected earthquake sources. However, while the most hazardous earthquakes on Earth occur underwater, most seismological stations are located on-land; precious seconds may go by before these earthquakes are detected. In this work, we harness available optical fiber infrastructure for EEW using the novel approach of Distributed Acoustic Sensing (DAS). DAS strain measurements of earthquakes from different regions are converted to ground motions using a real-time slant-stack approach, magnitudes are estimated using a theoretical earthquake source model, and ground shaking intensities are predicted via ground motion prediction equations. The results demonstrate the robustness of DAS-based EEW and the significant time-gains that can be achieved compared to the use of standard seismometers, in particular for offshore earthquakes.

Introduction

While earthquake prediction remains out of reach, continuous seismic monitoring has enabled earthquake early warning (EEW) systems that provide alerts to population centers and critical infrastructure seconds to tens of seconds before intense ground shaking is felt¹⁻⁴. Following rupture initiation, warning may be issued by analyzing recorded ground motions in real-time to assess the earthquake's damage potential. The performance of EEW systems largely depends on the spatial distribution of available seismic sensors⁵; for fast and robust warning issuance, seismic instruments should be densely installed in great proximity to active faults, where earthquakes are expected to occur. While most of the largest and most hazardous

earthquakes on Earth occur offshore in subduction zones, the vast majority of seismic stations are located on-land. Thus, valuable time may be lost waiting for seismic waves to reach on-land stations⁶. Current solutions, such as densifying on-land seismic networks and installing cabled ocean bottom sensor networks, are implemented in Japan⁷ where the seismic risk is high. However, high costs preclude their worldwide implementation. An alternative is to convert fiber optic cables into dense seismic networks via the novel technology of Distributed Acoustic Sensing (DAS)^{8,9}. The ever-growing worldwide deployment of optical fiber telecommunication infrastructure, in particular submarine cables, opens opportunities for widespread low-cost implementation of DAS for EEW, circumventing costly ocean-bottom deployments and operations. The potential of seafloor DAS for EEW has not been quantitatively demonstrated yet, a gap addressed in this work.

Over the past several years, the unique advantages of DAS have proven valuable for various seismological purposes including earthquake analysis¹⁰⁻¹² and subsurface imaging¹³⁻¹⁶. DAS has key features that are ideally suited for the challenges of EEW. It facilitates spatially and temporally continuous seismic measurements at hard-to-reach places, such as underwater¹⁷ and in boreholes¹⁸, closer to earthquake hypocenters. Recordings are obtained at meter spacings along tens-of-kilometers long fibers, essentially transforming any optical fiber into a dense seismic array. By using DAS, signal to noise is enhanced¹¹ and earthquakes are easily distinguishable from noise¹⁹. Furthermore, the DAS interrogator is sensing the whole fiber from one of its ends, nullifying power and telemetry considerations to distant fiber segments. Thus, the use of optical fibers as dense seismic networks could be decisive in the performance of EEW systems, significantly improving earthquake warning times and allowing for better preparedness for intense shaking.

In this work, we propose the first scheme for harnessing DAS for EEW. Early warning is typically achieved by 1) detecting an earthquake, 2) determining its location, 3) resolving the earthquake source parameters (magnitude and stress drop), and 4) predicting ground shaking intensities, typically peak ground velocities (PGV) and peak ground accelerations (PGA). To the best of our knowledge, these four real-time objectives are yet to be addressed. Real-time earthquake detection and location may be achieved using either well-established seismometer-based approaches^{20–23} applied to single or multiple DAS channels, or array processing techniques such as beamforming^{12,24–26}. While detection can be achieved with relative ease even with seismometer-based algorithms^{20,23}, earthquake location poses several challenges that are unique to DAS data^{12,27}. DAS measurements are extremely sensitive to local subsurface heterogeneities and the recorded strain wavefield may not be coherent enough for reliable earthquake location or may be dominated by scattered waves. In addition, the location of the fiber may not be known accurately. These hindrances will be considered when devising real-time earthquake location schemes, a subject of subsequent manuscripts. Here, we address the last two objectives: real-time magnitude estimation and shaking intensity prediction.

Most operational EEW systems rely on empirical relations for both magnitude estimation and ground motion prediction^{28,29}. The robustness of these relations largely relies on the quality, quantity, and magnitude range of available earthquake observations³⁰. Since DAS is a relatively new seismic measurement technology⁸, current earthquake DAS datasets are insufficient to devise robust empirical methods, and a physics-based approach that does not rely on data availability should be developed^{30–32}. Recently, a holistic physics-based approach for earthquake source parameter (magnitude and stress drop) estimation and ground motion prediction has been proposed³⁰. A similar method, adapted to DAS data, is developed here by deriving a theoretical

expression for real-time magnitude estimation using the root-mean-squares (rms) of ground accelerations.

Since DAS measures strains (or strain-rates) and earthquake magnitude is directly related to ground motions (displacements, velocities and accelerations)³³, DAS measurements first need to be converted to ground motions³⁴. This objective is typically achieved by using the apparent slowness (reciprocal of velocity), p_x , measured along the fiber³⁵:

$$\frac{d^n}{dt^n} D(t) = \frac{d^{n-1}}{dt^{n-1}} \epsilon(t) / p_x, \quad (1)$$

where $\epsilon(t)$ and $D(t)$ are the time-series of strains and ground displacements, respectively, and n equals 0, 1 or 2 corresponds to conversions to ground displacements, velocities or accelerations, respectively. Slowness has been observed to change rapidly both in time and space (along the fiber): temporal variations are due to velocity differences among recorded seismic phases (i.e., P-, S-, scattered-, surface-waves)³⁴ and spatial variations are a result of lateral subsurface-velocity heterogeneities, that may be significant and abrupt^{11,12,16,27}. Accurate conversion of strain-rates to ground accelerations requires that slowness be resolved as a function of both time and space. Recently, a slant-stack based strains to ground motion conversion method has been proposed³⁴, and is modified and adapted here for real-time processing.

The approaches presented in this manuscript build on the above-mentioned advancements in physics-based EEW³⁰ and DAS earthquake data processing³⁴. The potential of the modified strains to ground motions conversion and the new magnitude expression for EEW are examined in conjunction with a theoretical ground motion prediction equation (GMPE)³⁶. To this end, we compiled a DAS earthquake dataset from different tectonic environments. In the following sections, we present and validate a computationally efficient real-time protocol that relies on

straightforward analytical formulations for the analysis of DAS recorded earthquakes. Strain-rates are converted to ground accelerations and earthquake magnitude is estimated using several well-coupled fiber segments along different ocean-bottom fibers. The magnitude is then used to predict PGV and PGA away from the hypocenter. Magnitude and peak ground shaking predictions are continuously updated and modified as new seismic signals are recorded. We demonstrate the robustness of these real-time approaches for a wide magnitude range and show that using offshore fibers for EEW can significantly improve warning times compared to those expected from standard seismometer-based EEW systems.

Results

Using DAS data for magnitude estimation

Ideally, magnitude should be estimated using seismic recordings of ground displacements, D , rather than ground velocities, V , or accelerations, A , and the signals should include as much of their low-frequency portion as possible to avoid magnitude saturation^{31,33}. Ground displacements can be obtained from DAS measurements by integrating strain measurements in time (or double integration of strain-rates) and dividing them by the slowness ($n=0$ in Eq. 1). However, the use of DAS converted ground displacements is challenging given the inherently high instrumental noise levels, especially at large distances along long fibers^{9,11,37}. The behavior of DAS instrumental noise is demonstrated in Fig. (1) for an earthquake of magnitude 3.6 recorded at a distance of 135 km from an optical fiber offshore southeastern Greece^{11,16,34,38} (See map in Supplementary Fig. 1). At low frequencies, the instrumental noise of the time-integral of strains ($\propto D$, Fig. 1a, b), strains ($\propto V$, Fig. 1c, d) and strain-rates ($\propto A$, Fig. 1e, f) is proportional to f^{-2} , f^{-1} and independent of frequency, f , respectively. As a result, strains-

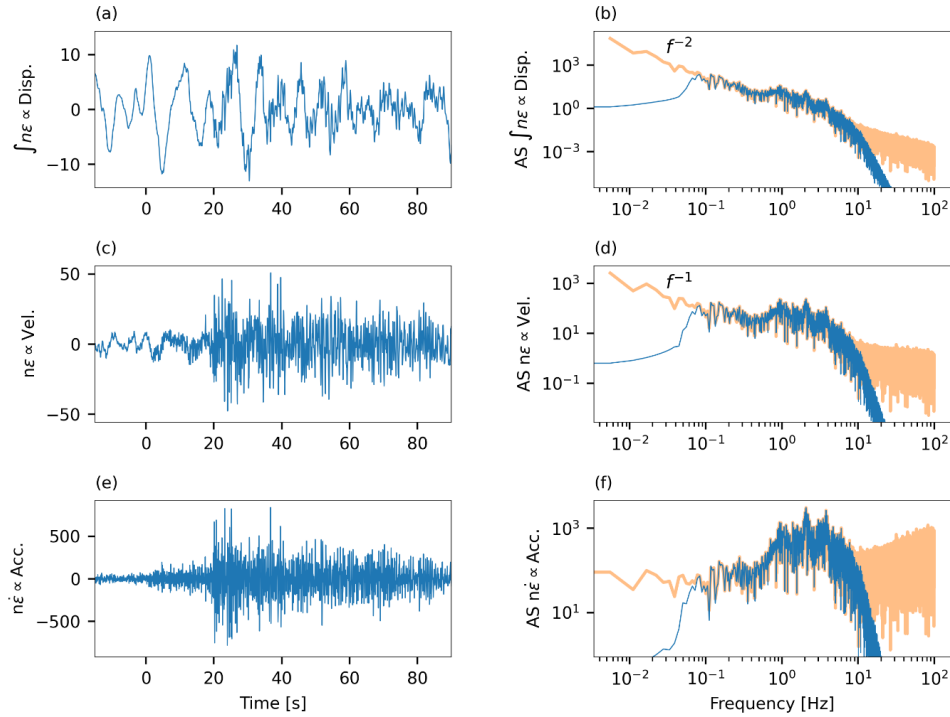


Fig. 1 DAS instrumental noise. **a-b** Strains-integral, **c-d** strains, and **e-f** strain-rates of a magnitude 3.6 earthquake recorded at a hypocentral distance of 135 km at 21 km along a fiber offshore Greece. Signals filtered between 0.06 and 10 Hz are shown on the left (**a**, **c**, **e**) and the corresponding spectra are shown on the right (blue curves **b**, **d**, **f**). The prefiltered spectra (orange curves **b**, **d**, **f**) demonstrate that low frequency noise is **b** $\propto f^{-2}$, **d** $\propto f^{-1}$, and **f** independent of frequency.

integral ($\propto D$, Fig. 1a) and strains ($\propto V$, Fig. 1c) time-series are contaminated by low-frequency noise, and their use may lead to magnitude over-estimation and false alarms. Thus, we only use strain-rates ($\propto A$) for real-time magnitude estimation even though they present a weaker correlation with earthquake magnitude compared to strains-integral ($\propto D$) and strains ($\propto V$) (See “The relation between earthquake source parameters and ground motions” in Methods). Since strain-rates’ instrumental noise increases as f at high frequencies (Fig. 1f), a lowpass filter is needed. This filter will not bias magnitude estimations because larger earthquakes produce lower frequency radiation.

Strain-rates to ground accelerations conversion

The performance of the conversion algorithm (See “Real-time strain-rates to ground accelerations conversion” in Methods) is demonstrated for a magnitude 3.8 earthquake recorded offshore Chile at a hypocentral distance of 60 km (See map in Supplementary Fig. 1) for a single DAS channel at a distance of 103 km along the fiber (Fig. 2). Note that direct P-waves are not visible, although P-wave induced scattered-waves are clearly seen (1-6 s in Fig. 2a, b). The same analysis for the largest earthquake in the dataset, a magnitude 5.7, is shown in Supplementary Fig. (2); for this earthquake, strain-rate amplitudes exhibit some saturation (See Discussion). The real-time slant-stack approach resolves the apparent velocities of the different seismic phases: ~ 4.2 km/s for direct S-waves (6-9 s in Fig. 2a, b) and ~ 1.8 km/s for scattered- and surface-waves (e.g., 1-6 s and 10-13 s in Fig. 2a, b). Owing to these velocity variations, ground accelerations are somewhat different from strain-rates: the former (blue curve in Fig. 2c) exhibit a noticeable amplitude difference between fast S-waves and slow scattered- and surface-waves, while the latter (black curve in Fig. 2c) display similar amplitudes for both phases. A comparison between the performance of the real-time slant-stack conversion and the previously presented approach³⁴ indicates that the real-time adaptations do not decrease the conversion quality (Supplementary Fig. 3).

The effect of stress drop variability

Stress drop, $\Delta\tau$, is a fundamental earthquake source parameter that strongly affects ground motion intensities^{36,39–41} (See “The relation between earthquake source parameters and ground motions” in Methods). For optimal ground motion prediction, both magnitude and stress drop should be determined, as demonstrated by recent studies^{2,30,32,36}. Since in this framework we only use one ground motion metric, i.e., ground accelerations rms, A_{rms} , we may only estimate

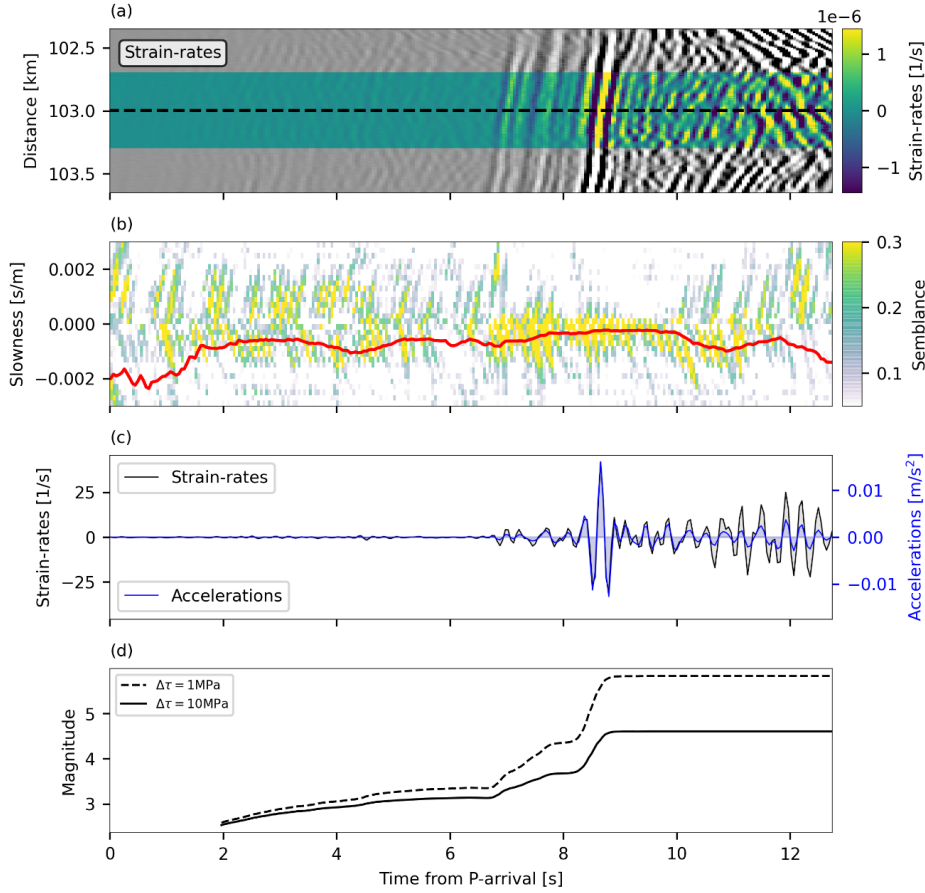


Fig. 2 Strain-rates to ground accelerations conversion and magnitude estimation. **a** Strain-rates of a magnitude 3.8 earthquake recorded at a hypocentral distance of 60 km between 102.3 km and 103.6 km along a fiber offshore Chile. The fiber segment used for magnitude estimation is color-coded (102.7 km to 103.3 km). **b** Semblance as functions of apparent slowness and time from P-wave arrival for a reference DAS channel at 103 km from the interrogator (black dashed line in **a**). Smoothed slowness (See Methods) is indicated by a red curve. **c** Strain-rates (black) and converted ground accelerations (blues) for the reference DAS channel. **d** Real-time magnitude evolution using stress drops of 1 MPa (dashed curve) and 10 MPa (solid curve).

the magnitude (see “Magnitude estimation from bandlimited ground accelerations” in Methods) while the stress drop needs to be set a priori. Because A_{rms} are highly affected by the stress drop, and because its a priori value may deviate from its earthquake-specific real value^{36,42}, it is useful to examine the effect of stress drop variability on magnitude estimation and intense shaking prediction. To this end, we synthesized A_{rms} using an ideal lowpass Butterworth filter, and

PGV_{synt} and PGA_{synt} for different magnitudes using $\Delta\tau = 10$ MPa at a hypocentral distance of 50 km (See “Synthetic ground motions” in Methods). We then used the synthetic A_{rms} to estimate the magnitudes, using different a priori stress drops of 1, 10 and 100 MPa (Eq. 7). The estimated magnitude and a priori stress drop were then used to predict PGV_{pred} and PGA_{pred} (Eq. 10), assuming that the distance is known (Fig. 3). When using $\Delta\tau = 10$ MPa in Eq. (7) and (10), magnitude, PGV, and PGA discrepancies are small (panels b, d and f of Fig. 3, respectively) and mostly attributed to the approximations made in deriving Eq. (7) (See Supplementary Note 1). When the stress drop in Eq. (7) is under-estimated ($\Delta\tau = 1$ MPa) and over-estimated ($\Delta\tau = 100$ MPa), magnitudes are over-estimated and under-estimated, respectively, by as much as 1.33 magnitude units for large earthquakes (Fig. 3a). When these biased magnitudes are used to predict PGV, and PGA, they result in reasonable predictions: the standard deviations of the residuals are limited to $\sim 0.43 \log_{10}(PGV)$ and $\log_{10}(PGA)$ units (solid curves in Fig. 3c, e, respectively). However, if synthetic magnitudes are used in conjunction with the over- and under-estimated stress drops, PGV and PGA discrepancies would be significantly higher (dashed curves in Fig. 3c, e). Further explanations on the shape of the residual plots are provided in Supplementary Note 2.

The results in Fig. (3) show that while the discrepancies between the synthetic earthquake stress drop and that used in Eq. (7) may have a significant impact on magnitude estimation, the effect on ground motion prediction is minimized, and the approach may be reliably used even with a biased stress drop. The effect of stress drop variability will be further examined using recorded earthquakes in the following section.

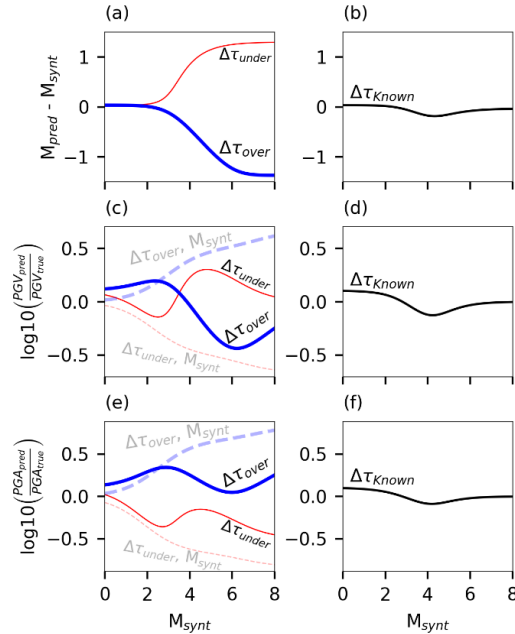


Fig. 3 The effect of stress drop variability on magnitude estimation and ground motion prediction. Estimated minus synthetic magnitude as a function of synthetic magnitude for **a** under-estimated (1 MPa), over-estimated (100 MPa) and **b** known (10 MPa) stress drops. The logarithms of predicted peak ground motions minus the logarithms of synthetic peak ground motions as functions of synthetic magnitude are shown for PGV for **c** 1 MPa and 100 MPa and **d** 10 MPa, and for PGA for **e** 1 MPa and 100 MPa and **f** 10 MPa. The effect of using synthetic magnitude on **c** PGV and **e** PGA discrepancies is indicated by semi-transparent dashed curves. In all panels, curves corresponding to 1, 10 and 100 MPa are indicated by red, black and blue curves, respectively.

Real-time magnitude estimation and peak ground shaking prediction

The performance of the real-time strain-rates to ground accelerations conversion, magnitude estimation, and ground motion prediction are demonstrated using a composite earthquake catalog of 53 DAS and seismometer recorded earthquakes from Greece, France, and Chile (See “Earthquake dataset” in Methods, earthquake catalog in Supplementary Table 1, and maps showing the locations of earthquakes, fibers, and seismometers in Supplementary Fig. 1). These earthquakes range from magnitude 2 to 5.7 (Supplementary Fig. 4) and were recorded by four different offshore fibers using three different DAS interrogators. DAS records are converted

to ground accelerations and used to estimate the magnitude, while seismometer records are used to compare observed and predicted PGV and PGA. Earthquake locations (and hypocentral distances) and P- and S-wave arrival times are assumed to be known: the former are extracted from available earthquake catalogs and the latter are manually picked. In practice, earthquake location and phase picking will be achieved in real-time via additional modules, whose development is beyond the scope of this manuscript.

An initial magnitude estimate is obtained two seconds following P-wave detection at the first fiber segment, and is continuously updated with increasing data intervals and as the earthquake is recorded at additional locations along the fiber. Real-time magnitude estimation is demonstrated for an M3.8 earthquake using a single fiber segment in Fig. (2d). Magnitude increases with time, starting at the scattered P-waves (2-7 s), followed by a significant increase with the S-wave arrivals (7-9.5 s). As theoretically predicted (Fig. 3), magnitude estimates vary for different a priori stress drops, with magnitudes of 5.8 and 4.6 for 1 and 10 MPa, respectively, at 9.5 s from P-wave detection. Similar behavior is observed for the M5.7 earthquake shown in Supplementary Fig. (2d). Magnitude estimates improve with time as seen in Fig. (4a-c) where real-time and catalog magnitudes are compared at 4, 10 and 15 s from the first P-wave detection, for the entire dataset.

A comparison between predicted (Eq. 10) and observed (See “Earthquake dataset” in Methods) PGV and PGA at 15 s indicates that the residuals are independent of hypocentral distance (Fig. 4d, e and Supplementary Fig. 5d, e) and magnitude (Supplementary Fig. 6d, e), and that their standard deviations are relatively small, only slightly higher than the optimal values, i.e., within-event variabilities reported in the caption of Fig. (4). The latter result suggests that peak ground motion residuals are mainly caused by different site and path conditions that

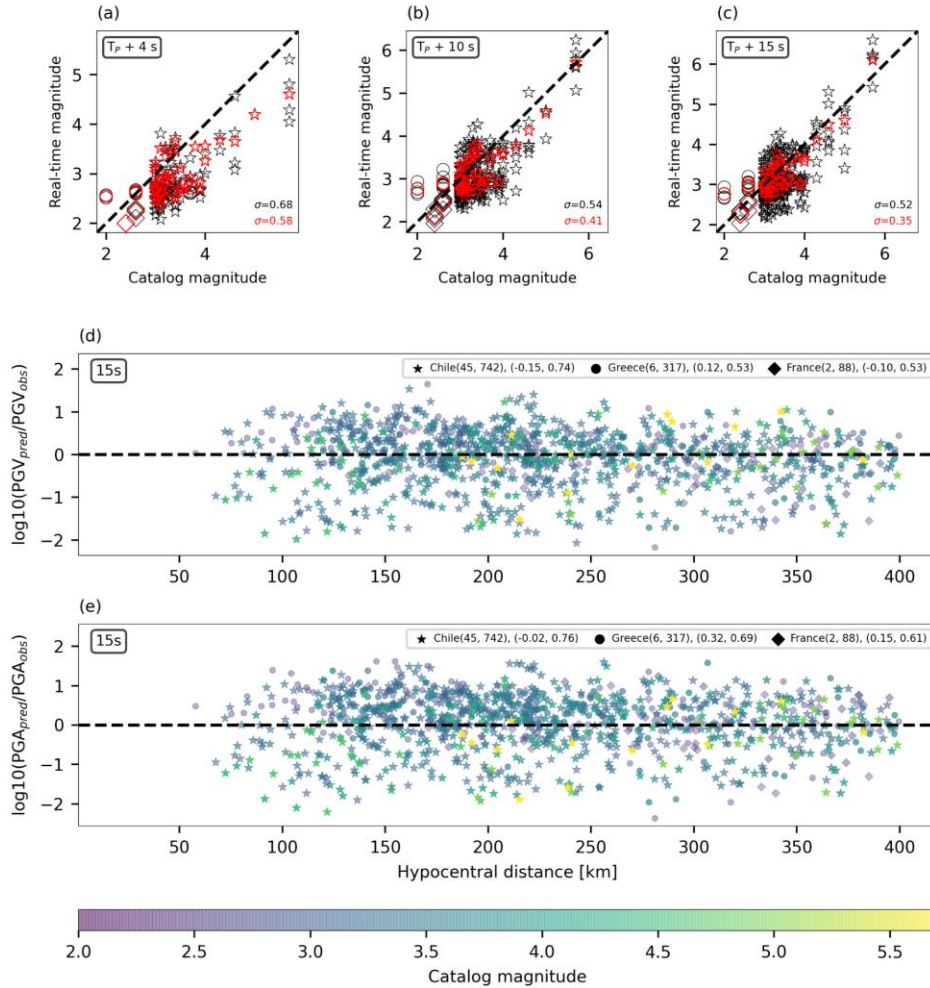


Fig. 4 Real-time magnitude estimation and ground motion prediction using 10 MPa. Real-time magnitude as a function of catalog magnitude at **a** 4, **b** 10 and **c** 15 seconds from the P-wave arrival at the first fiber segment. Fiber-segment-specific estimates and event averages are indicated by black and red symbols, respectively. The dashed black line is a 1:1 line and the standard deviations of the magnitude residuals are indicated in the bottom right corners for segment specific (black) and event averaged (red) estimates. Discrepancies between the logarithms of predicted and observed peak ground motions are plotted for **d** PGV and **e** PGA as functions of hypocentral distance. Color-code corresponds to catalog magnitudes. Earthquakes from Chile, Greece and France are indicated by stars, circles and triangles, respectively. Panel legends indicate the following: cable name (number of earthquakes, number of PGV and PGA observations), (average residuals, standard deviation to the residuals). Average within event variabilities, i.e., the optimal standard deviation to the residuals, for PGV are 0.68, 0.5 and 0.52 for Chile, Greece and France, respectively, and for PGA are 0.71, 0.61 and 0.59 for Chile, Greece and France, respectively.

may be accounted for in future implementations, subject to additional research. While magnitude estimates are highly sensitive to the a priori stress drop, PGV and PGA residuals exhibit low

sensitivity (Fig. 4 and Supplementary Fig. 5 for 10 and 1 MPa, respectively). This behavior is further demonstrated by examining the average magnitude, and PGV and PGA residuals for the largest available earthquake (Supplementary Fig. 7): average residuals show little sensitivity to stress drop and similar trends to those theoretically predicted (Fig. 3), i.e., PGV residuals are higher for stress drop under-estimation, and PGA residuals are lower for stress drop under-estimation.

Discussion

The results presented in this manuscript demonstrate that DAS can be reliably used for real-time magnitude estimation and ground motion prediction, two critical components of an operational EEW system. The use of DAS for EEW presents several significant advantages compared to the use of standard seismometers, especially in the time-gain for offshore earthquakes. This latter advantage is illustrated in Fig. (5) using the fiber deployed offshore Chile, where ocean-bottom earthquakes pose a significant seismic hazard. For the offshore earthquakes shown in Fig. (5a), by the time S-waves are expected to reach the Chilean coastline, real-time magnitude estimates are typically within half a magnitude unit of catalog values, allowing for robust alert issuance before intense ground shaking is felt onland, and well before earthquakes are recorded by the available seismic network (Fig. 5b). The time-gain achieved by using the offshore Chile fiber compared to the current seismometer network is defined here as the difference between the P-wave arrival at the closest fiber segment and at the fourth seismic station, as commonly required by EEW systems⁴³. This time-gain may be as large as 25 s for earthquakes that occur near the fiber and may even result in early detection and alert issuance for onland earthquakes where seismometer coverage is sparse (Fig. 5b). These precious seconds can

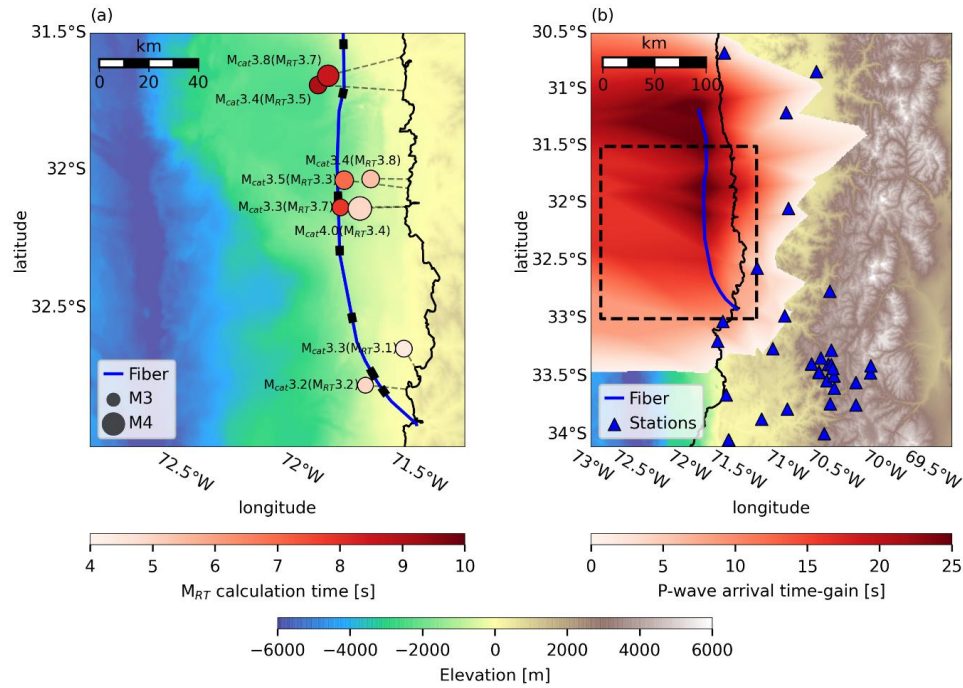


Fig. 5 Time-gain using offshore DAS. **a** Catalog (M_{cat}) and real-time (M_{RT}) magnitude estimates when S-waves are expected to reach the Chilean coastline. Earthquakes are indicated by circles with size corresponding to catalog magnitudes, and color corresponding to M_{RT} estimation times. The shortest path to the coastline is indicated by grey dashed lines for each earthquake. The fiber is indicated by a blue curve and fiber segments used for magnitude estimation are indicated by black rectangles. **b** P-wave time-gain (red color scale) for different possible earthquake locations; only positive time-gains are shown. Seismometers are indicated by blue triangles. The region shown in **a** is indicated by a black dashed rectangle in **b**.

have a decisive impact in mitigating the risk posed by potentially catastrophic offshore earthquakes.

Together with the time-gain for offshore earthquakes, DAS-based EEW is expected to outperform seismometer-based EEW for several reasons. Magnitude estimates are more reliable since data from many closely spaced DAS channels are averaged, reducing the impact of outliers and smoothing local effects. DAS facilitates robust differentiation between earthquakes and noise since earthquakes' seismic wavefield is near-instantaneously recorded on hundreds-of-meters long fiber segments. As a result, false detections will be reduced and one fiber segment may be sufficient to issue early warning, subject to earthquake location capabilities.

While direct S-waves are detected by horizontally installed fibers, direct P-waves are usually not (Fig. 2a), a result of their fast velocities and the angle between the waves' polarization and the fiber's axis^{11,44}. However, P-wave induced scattered-waves are well recorded (2-6 s in Fig. 2a, b) and used for magnitude estimation. The dominance of these scattered waves will pose difficulties for earthquake location, since using scattered P-waves instead of direct P-waves will likely point to the scatterers' locations rather than the earthquake's source. Because P-wave based magnitudes are typically under-estimated (Fig. 2d), they are not expected to cause false alarms, yet they may be sufficient to surpass predefined alert thresholds. The closer the fiber is to earthquake locations, the sooner the reliably recorded S-waves are detected and used.

The derivation of the presented physics-based magnitude estimation approach did not require any earthquake observations, a significant advantage since the scarcity of DAS earthquake observations hinders the derivation of empirical methods. Because no earthquakes were required, the approach is geographically independent and readily applicable in any tectonic setting using both offshore and onland fibers, as demonstrated here using earthquakes from Greece, France and Chile. Earthquake observations are only required to map well-coupled fiber segments, although this objective may also be achieved using ambient noise¹⁶. Using segments that are not well-coupled may lead to either magnitude under-estimation, if strain amplitudes are weak, or over-estimation, if a segment is suspended and experiences strong vibrations due to cable-waves⁴⁵. The approach allows for continuous update of magnitude and ground motion predictions, key for analyzing large earthquakes with long durations. In addition, using a holistic magnitude estimation and ground motion prediction that are derived from the same earthquake

model reduces the impact of stress drop related magnitude biases on ground motion predictions and enhances the overall robustness of the system.

The computational costs of the presented approaches are low. We analyzed 180 s long recordings of DAS fiber segments (33 channels), down-sampled to ~ 20 Hz, in ~ 136 s using a Python code on an Intel Core i7 laptop with 32 GB RAM using a single thread. Slant-stack computations are the most time-consuming (~ 4 s per channel) and can be parallelized for real-time implementations.

For few earthquakes, strain amplitudes exhibited a small degree of saturation. Nevertheless, magnitude estimations still allow for reliable ground motion predictions (Fig. 4). This phenomenon needs to be quantified and addressed as it may affect the ability to analyze higher strain amplitudes and provide reliable warnings for larger earthquakes.

The framework presented in this study demonstrates the great potential of using DAS for EEW. The approaches presented here allow for easy, robust, and fast implementation of EEW using both offshore and onland optical fibers in any tectonic setting. Specifically, using existing ocean-bottom optical fibers, which are almost ubiquitous along subduction zones worldwide, provide a cheap and readily available EEW solution, especially for exposed developing countries, that will significantly enhance earthquake hazard mitigation capabilities.

Methods

The relation between earthquake source parameters and ground motions

For large earthquakes recorded in the far-field, ground displacements root-mean-squares (rms), D_{rms} , are mostly a function of the seismic moment, M_0 : $D_{rms} \propto M_0^{5/6} \Delta\tau^{1/6}$ while ground

velocities rms, V_{rms} , and accelerations rms, A_{rms} , are also strongly influenced by the stress drop, $\Delta\tau$: $V_{rms} \propto M_0^{1/2} \Delta\tau^{1/2}$ and $A_{rms} \propto M_0^{1/3} \Delta\tau^{2/3}$ (Lior and Ziv, 2018, 2020). Note the different powers associated with M_0 and $\Delta\tau$. Thus, ground displacements serve as a better magnitude predictor compared to velocities or accelerations^{28,31,36}.

Real-time strain-rates to ground accelerations conversion

The slant-stack⁴⁶ based strains to ground motions conversion scheme³⁴ accounts for apparent phase velocity variations in both time and space. The conversion is applied for each DAS channel along the fiber using short, approximately linear, fiber segments. Here, this recently presented approach³⁴ is modified and optimized for real-time performance. The semblance (coherency) as a function of apparent slowness p_x and time t , for a DAS channel located at x_0 along the fiber, can be written as:

$$sem(p_x, t) = \frac{1}{L} \begin{cases} \frac{[\sum_{j=-L}^{-1} g(t+p_x(x_j-x_0))]^2}{\sum_{j=-L}^{-1} g(t+p_x(x_j-x_0))^2} & \text{if } p_x > 0 \\ \frac{[\sum_{j=1}^L g(t+p_x(x_j-x_0))]^2}{\sum_{j=1}^L g(t+p_x(x_j-x_0))^2} & \text{if } p_x < 0 \end{cases}, \quad (2)$$

where L is the number of DAS channels used for slowness estimation, $g(t)$ is the DAS strain-rates time-series, and $x_j - x_0$ is the distance between station j and the reference channel (at x_0). Equation (2) can be regarded as the causal slant-stack, where only data samples of $g(t)$ that have already been recorded are considered.

The conversion procedure is performed as follows. For computational efficiency, recorded strain-rates are down-sampled to 20 Hz (or slightly higher, depending on the original signals' sampling-rate). Data is lowpass filtered at 5 Hz using a 4-pole Butterworth filter to diminish high frequency instrumental noise. The applied down-sampling and filtering did not

decrease the robustness of the conversion and subsequent magnitude estimation. The local slant-stack transform is applied using fiber segments of ~ 380 m length³⁴, with channel spacings of ~ 20 m, skipping several channels for densely spaced measurements. The used fiber segments are long enough to resolve long seismic wavelengths with fast velocities of several km/s, and short enough so that seismic waves are coherent and fiber sections are approximately linear³⁴.

Semblance is calculated using 50 predefined slowness values, equally spaced between -5 s/km and 5 s/km. At each t , the wavefield's slowness is determined as the one with highest semblance. The produced slowness time-series is then smoothed by applying a causal moving-mean filter of 1 s to its absolute value. Strain-rates time-series are then divided by the slowness time-series to obtain ground accelerations, followed by an additional 5 Hz lowpass filter. Because we are eventually interested in the converted strain-rates' rms, the slowness' sign may be discarded (See "Magnitude estimation from bandlimited ground accelerations" in Methods).

Magnitude estimation from bandlimited ground accelerations

We derive an expression for the rms of the ground accelerations using the commonly used omega-squared source model⁴⁷ describing the far-field body wave spectra (grey dashed curve in Supplementary Fig. 8). This derivation procedure follows that used by several previous studies^{30,31,36,48-51}. The acceleration omega-squared model⁴⁷ subject to high frequency attenuation⁵² (grey dotted curve in Supplementary Fig. 8) reads as:

$$\ddot{\Omega}(f) = (2\pi f)^2 \frac{\Omega_0}{1 + \left(\frac{f}{f_0}\right)^2} e^{-\pi\kappa f}, \quad (3)$$

where f_0 is the source corner frequency, Ω_0 is the displacement low frequency spectral plateau, and κ is an attenuation parameter. Since strain-rates are lowpass filtered at 5 Hz, acceleration rms

are calculated using Eq. (3) as $A_{rms} = \sqrt{\frac{2}{T} \int_{f=0}^{f=5} |\ddot{\Omega}(f)|^2 df}$ (black dashed curve in Supplementary

Fig. 8), where T is the data interval. The integral is solved and an analytic approximation is obtained (See Supplementary Note 1). The spectral parameters Ω_0 and f_0 are substituted with the seismic moment³³ and stress drop⁵³, respectively, via:

$$M_0 = \Omega_0 \frac{4\pi\rho C^3 R}{U_{\varphi\theta} F_S}, \quad (4a)$$

$$\Delta\tau = \frac{7}{16} M_0 \left(\frac{f_0}{kC_S} \right)^3, \quad (4b)$$

where ρ is the density at the source, C is the wave velocity at the source (C_P and C_S for P- and S-waves, respectively), R is the hypocentral distance, $U_{\varphi\theta}$ is the average radiation pattern, F_S is the free-surface correction, and k is a phase-specific constant which also depends on the source model and rupture speed⁵⁴. Equation (4b) is valid for a circular crack embedded in a homogeneous medium⁵³. The resulting expression is:

$$A_{rms}^{approx} = A_1 M_0^{1/3} \Delta\tau^{2/3} \sqrt{1 - e^{-2\alpha_m}} \frac{1}{R\sqrt{\kappa T} \left(1 + A_2^2 \kappa^2 \left(\frac{\Delta\tau}{M_0} \right)^{2/3} \sqrt{1 - e^{-2\alpha_m}} / h(\alpha_m) \right)}, \quad (5)$$

where the superscript *approx* signifies approximate rms, $A_1 = \frac{U_{\varphi\theta} F_S \sqrt{\pi}}{\rho C^3} \left(\frac{16}{7} \right)^{2/3} (kC_S)^2$, $A_2 =$

$$\pi \left(\frac{16}{7} \right)^{1/3} kC_S, \quad h(\alpha_m) = e^{-\alpha_m} \sqrt{\frac{1}{2} [-3 - 6\alpha_m - 6\alpha_m^2 - 4\alpha_m^3 - 2\alpha_m^4 + 3e^{2\alpha_m}]}$$
 and $\alpha_m = 5\pi\kappa$.

Equation (5) can be analytically solved for the seismic moment:

$$M_0 = \frac{1}{27a_1} \left(\frac{a_4}{2^{1/3}} + \frac{2^{1/3}a_2^2}{a_4} + a_2 \right)^3, \quad (6)$$

where $a_1 = A_1 \Delta\tau^{2/3} \sqrt{1 - e^{-2\alpha_m}} \frac{1}{R\sqrt{\kappa T}}$, $a_2 = A_{rms}$, $a_3 = A_{rms} A_2^2 \Delta\tau^{2/3} \kappa^2 \sqrt{1 - e^{-2\alpha_m}} / h(\alpha_m)$

and $a_4 = \left(3\sqrt{3(27a_1^4 a_3^2 + 4a_1^2 a_2^3 a_3)} + 27a_1^2 a_3 + 2a_2^3 \right)^{1/3}$. The moment magnitude can then be

written as:

$$M_W = 2 \log_{10} \left(\frac{a_4}{2^{1/3}} + \frac{2^{1/3} a_2^2}{a_4} + a_2 \right) - \frac{2}{3} \log_{10}(a_1) - 7.05, \quad (7)$$

where M_0 is expressed in Nm.

While the coefficients a_1 , a_2 , a_3 and a_4 contain many parameters, only few are updated in real-time: A_{rms} is continuously updated as new data is recorded, the available data interval T begins at the P-wave arrival and increases with time, and R is updated as earthquake location improves. The parameters used are³⁰: $F_S = 2$, $\rho = 2600 \text{ kg/m}^3$, $C_S = 3.2 \text{ km/s}$, $C_P = 5.3 \text{ km/s}$, $\kappa = 0.025 \text{ s}$, $U_{\phi\theta}$ equals 0.52 and 0.63 for P- and S-waves, respectively³³, and k equals 0.32 and 0.21 for P- and S-waves, respectively⁵⁴. For data intervals that contain both P- and S-waves, the phase specific constants need to be averaged based on the relative intervals of each phase³⁰:

$$const = \frac{T_{S-P}}{T} const_P + \frac{T-T_{S-P}}{T} const_S, \quad (8)$$

where $const$ stands for $U_{\phi\theta}$, C or k for P- or S-waves, and T_{S-P} is the S-P data interval. Using these parameters, a_1 and a_3 may be written as:

$$a_1 = 113014 \left(\frac{k^2 U_{\phi\theta}}{C^3} \right) \Delta\tau^{2/3} \frac{1}{R\sqrt{T}}, \quad (9a)$$

$$a_3 = 1828968 (k^2) \Delta\tau^{2/3} A_{rms}, \quad (9b)$$

where phase-specific terms are written in parentheses.

In this application, the magnitude is estimated using several manually identified well-coupled fiber segments of ~600 m as follows. Strain-rates within each fiber segment are converted to ground accelerations (See “Real-time strain-rates to ground accelerations conversion” in Methods). A_{rms} is calculated per DAS channel starting at the P-wave arrival, and is then logarithmically averaged per fiber segment at every time-step to minimize the impact of

outliers. Since DAS can only measure the wavefield in-line with the fiber, A_{rms} is multiplied by $\sqrt{2}$ to compensate for the missing orthogonal component. The averaged A_{rms} at time T is then input to Eq. (7) along with $\Delta\tau$ and R to estimate the magnitude. Magnitude estimates are continuously updated until either averaged A_{rms} reaches its maximum value, or $T = 60$ seconds³⁰. Magnitude estimates from different fiber segments are weight-averaged by the available data interval to obtain an event specific estimate.

Ground motion prediction

For PGV and PGA prediction, we use a set of physics-based GMPEs^{30,36}, derived using the same source model⁴⁷ (Eq. 3) used to obtain the real-time magnitude expression (Eq. 7) (See ‘‘Magnitude estimation from bandlimited ground accelerations’’ in Methods). The GMPEs for PGV and PGA are:

$$PGV = 2.9\sqrt{M_0\Delta\tau} \frac{\beta_V}{R \sqrt{\frac{1}{kC_S} \left(\frac{7M_0}{16\Delta\tau}\right)^{1/3} + R/C_S \left[1 + \pi^{4/3} \kappa_0 kC_S \left(\frac{16\Delta\tau}{7M_0}\right)^{1/3}\right]^{3/2}}}, \quad (10a)$$

$$PGA = 3.3M_0^{1/3} \Delta\tau^{2/3} \frac{\beta_A}{R \sqrt{\kappa_0 \left[\frac{1}{kC_S} \left(\frac{7M_0}{16\Delta\tau}\right)^{1/3} + R/C_S\right] \left[1 + 1.5^{-1/4} \pi \kappa_0 kC_S \left(\frac{16\Delta\tau}{7M_0}\right)^{1/3}\right]^2}}, \quad (10b)$$

where $\beta_V = 2\pi U_{\phi\theta} F_s \sqrt{16/7} (kC_S)^{3/2} / (\sqrt{2\pi} 4\rho C_S^3)$ and $\beta_A = 4\pi U_{\phi\theta} F_s (16/7)^{2/3} (kC_S)^2 / (\sqrt{\pi} 4\rho C_S^3)$. These theoretical GMPEs are readily applicable in any seismic region. Using the parameter tuning for S-waves (See ‘‘Magnitude estimation from bandlimited ground accelerations’’ in Methods), $\beta_V = 2.44 \cdot 10^{-10} \text{ m}^{1.5} \text{ s}^{1.5} / \text{kg}$ and $\beta_A = 2.05 \cdot 10^{-8} \text{ m}^2 / \text{kg}^{30}$.

Synthetic ground motions

The GMPEs in Eq. (10) are used to generate synthetic PGV and PGA for different seismic moments, stress drops and hypocentral distances. Synthetic A_{rms} are generated by calculating the rms of the acceleration spectra (Supplementary Fig. 8). These spectra are produced for a specific seismic moment, stress drop and hypocentral distance using Eq. (3) and (4), subject to a lowpass filter. The filter is modeled in two manners: as a clean cutoff (dashed black curve in Supplementary Fig. 8) as used for the model derivation (See “Magnitude estimation from bandlimited ground accelerations” in Methods), or as an ideal 4-pole Butterworth filter (solid black curve in Supplementary Fig. 8), similar to that used for DAS signal processing.

Earthquake dataset

DAS data was recorded by four different ocean-bottom fibers, two offshore Greece^{11,16,34,38}, one offshore France^{11,17,34} and one offshore Chile. The measurements in Greece were conducted using a Febus A1 DAS interrogator between 18-19 and 19-25 April 2019 on 13.2 km and 26.2 km long fibers, sampled at 6 ms and 5 ms, respectively. Gauge length and spatial sampling were both set to 19.2 m for the two fibers. The measurements in France were conducted using an Aragon Photonics hDAS interrogator between 11-31 July 2019 on a 44.8 km long fiber, sampled at 10 ms and 2 ms for the first and last 10 days, respectively. Gauge length and spatial sampling were both set to 10 m. The measurements in Chile were conducted using an ASN OptoDAS interrogator between 27 October and 3 December 2021 on a 204 km long fiber, sampled at 8 ms. Gauge length and spatial sampling were both set to 4.085 m. The Febus and OptoDAS interrogators record strain-rates while the Aragon instrument records strains; the latter were differentiated to strain-rates before the conversion to ground accelerations.

Seismometer recordings were used to calculate PGV and PGA for the different earthquakes as follows. Data for Greece, France and Chile were obtained from the National Observatory of Athens, the RESIF repository and IRIS, respectively. Seismometers' two horizontal components were demeaned and highpass filtered at 1 Hz using a 4-pole Butterworth filter, followed by a simple gain correction. Velocity-meter signals were differentiated to obtain ground accelerations and accelerometer records were integrated to obtain ground velocities. An additional highpass filter was applied after differentiations and integrations. PGV (PGA) were then calculated as the geometric mean of the maximum of the absolute value of the two velocity (acceleration) components. PGV and PGA that are smaller than 5 times the standard deviation of the associated time-series are discarded as they may be biased by noise.

References

1. Allen, R. M. & Melgar, D. Earthquake Early Warning: Advances, Scientific Challenges, and Societal Needs. *Annu. Rev. Earth Planet. Sci.* **47**, 361–388 (2019).
2. Nof, R. N., Lior, I. & Kurzon, I. Earthquake Early Warning System in Israel—Towards an Operational Stage. *Front. Earth Sci.* **9**, (2021).
3. Colombelli, S., Festa, G. & Zollo, A. Early rupture signals predict the final earthquake size. *Geophys. J. Int.* **223**, 692–706 (2020).
4. Licciardi, A., Bletery, Q., Rouet-Leduc, B., Ampuero, J.-P. & Juhel, K. Instantaneous tracking of earthquake growth with elastogravity signals. *Nature* (2022) doi:10.1038/s41586-022-04672-7.
5. Kuyuk, H. S. & Allen, R. M. Optimal Seismic Network Density for Earthquake Early Warning: A Case Study from California. *Seismol. Res. Lett.* **84**, 946–954 (2013).
6. Wald, D. J. Practical limitations of earthquake early warning. *Earthq. Spectra* **36**, 1412–1447 (2020).
7. Aoi, S. *et al.* MOWLAS: NIED observation network for earthquake, tsunami and volcano. *Earth Planets Space* **72**, 126 (2020).

8. Zhan, Z. Distributed Acoustic Sensing Turns Fiber-Optic Cables into Sensitive Seismic Antennas. *Seismol. Res. Lett.* **91**, 1–15 (2020).
9. Fernandez-Ruiz, M. R. *et al.* Seismic Monitoring With Distributed Acoustic Sensing From the Near-Surface to the Deep Oceans. *J. Light. Technol.* **40**, 1453–1463 (2022).
10. Lindsey, N. J., Rademacher, H. & Ajo-Franklin, J. B. On the Broadband Instrument Response of Fiber-Optic DAS Arrays. *J. Geophys. Res. Solid Earth* **125**, (2020).
11. Lior, I. *et al.* On the Detection Capabilities of Underwater Distributed Acoustic Sensing. *J. Geophys. Res. Solid Earth* **126**, (2021).
12. van den Ende, M. P. A. & Ampuero, J.-P. Evaluating seismic beamforming capabilities of distributed acoustic sensing arrays. *Solid Earth* **12**, 915–934 (2021).
13. Spica, Z. J. *et al.* Subsurface Imaging With Ocean-Bottom Distributed Acoustic Sensing and Water Phases Reverberations. *Geophys. Res. Lett.* **49**, (2022).
14. Williams, E. F. *et al.* Scholte wave inversion and passive source imaging with ocean-bottom DAS. *Lead. Edge* **40**, 576–583 (2021).
15. Yuan, S., Lellouch, A., Clapp, R. G. & Biondi, B. Near-surface characterization using a roadside distributed acoustic sensing array. *Lead. Edge* **39**, 646–653 (2020).
16. Lior, I., Mercerat, E. D., Rivet, D., Sladen, A. & Ampuero, J.-P. Imaging an Underwater Basin and Its Resonance Modes Using Optical Fiber Distributed Acoustic Sensing. **12** (2022).
17. Sladen, A. *et al.* Distributed sensing of earthquakes and ocean-solid Earth interactions on seafloor telecom cables. *Nat. Commun.* **10**, 1–8 (2019).
18. Lellouch, A. & Biondi, B. L. Seismic Applications of Downhole DAS. *Sensors* **21**, 2897 (2021).
19. Li, Z. & Zhan, Z. Pushing the limit of earthquake detection with distributed acoustic sensing and template matching: a case study at the Brady geothermal field. *Geophys. J. Int.* **215**, 1583–1593 (2018).
20. Lomax, A., Satriano, C. & Vassallo, M. Automatic Picker Developments and Optimization: FilterPicker--a Robust, Broadband Picker for Real-Time Seismic Monitoring and Earthquake Early Warning. *Seismol. Res. Lett.* **83**, 531–540 (2012).

21. Satriano, C., Lomax, A. & Zollo, A. Real-Time Evolutionary Earthquake Location for Seismic Early Warning. *Bull. Seismol. Soc. Am.* **98**, 1482–1494 (2008).
22. Eisermann, A. S., Ziv, A. & Wust-Bloch, H. G. Array-Based Earthquake Location for Regional Earthquake Early Warning: Case Studies from the Dead Sea Transform. *Bull. Seismol. Soc. Am.* **108**, 2046–2053 (2018).
23. Li, Z., Meier, M.-A., Hauksson, E., Zhan, Z. & Andrews, J. Machine Learning Seismic Wave Discrimination: Application to Earthquake Early Warning. *Geophys. Res. Lett.* **45**, 4773–4779 (2018).
24. Rost, S. Array seismology: Methods and applications. *Rev. Geophys.* **40**, (2002).
25. Nayak, A., Ajo-Franklin, J., & the Imperial Valley Dark Fiber Team. Distributed Acoustic Sensing Using Dark Fiber for Array Detection of Regional Earthquakes. *Seismol. Res. Lett.* **92**, 2441–2452 (2021).
26. Lellouch, A., Yuan, S., Ellsworth, W. L. & Biondi, B. Velocity-Based Earthquake Detection Using Downhole Distributed Acoustic Sensing—Examples from the San Andreas Fault Observatory at Depth. *Bull. Seismol. Soc. Am.* **109**, 2491–2500 (2019).
27. Singh, S., Capdeville, Y. & Igel, H. Correcting wavefield gradients for the effects of local small-scale heterogeneities. *Geophys. J. Int.* **220**, 996–1011 (2020).
28. Kuyuk, H. S. & Allen, R. M. A global approach to provide magnitude estimates for earthquake early warning alerts: MAGNITUDE FOR EARTHQUAKE EARLY WARNING. *Geophys. Res. Lett.* **40**, 6329–6333 (2013).
29. Sadeh, M., Ziv, A. & Wust-Bloch, H. Real-time magnitude proxies for earthquake early warning in Israel. *Geophys. J. Int.* **196**, 939–950 (2014).
30. Lior, I. & Ziv, A. Generic Source Parameter Determination and Ground-Motion Prediction for Earthquake Early Warning. *Bull. Seismol. Soc. Am.* **110**, 345–356 (2020).
31. Lior, I., Ziv, A. & Madariaga, R. *P*-Wave Attenuation with Implications for Earthquake Early Warning. *Bull. Seismol. Soc. Am.* **106**, 13–22 (2016).
32. Ziv, A. & Lior, I. Real-Time Moment Magnitude and Stress Drop with Implications for Real-Time Shaking Prediction. *Bull. Seismol. Soc. Am.* **106**, 2459–2468 (2016).

33. Aki, K. & Richards, P. G. *Quantitative seismology*. (University Science Books, 2002).
34. Lior, I. *et al.* Strain to ground motion conversion of distributed acoustic sensing data for earthquake magnitude and stress drop determination. *Solid Earth* **12**, 1421–1442 (2021).
35. Daley, T. M., Miller, D. E., Dodds, K., Cook, P. & Freifeld, B. M. Field testing of modular borehole monitoring with simultaneous distributed acoustic sensing and geophone vertical seismic profiles at Citronelle, Alabama: Field testing of MBM. *Geophys. Prospect.* **64**, 1318–1334 (2016).
36. Lior, I. & Ziv, A. The Relation Between Ground Motion, Earthquake Source Parameters, and Attenuation: Implications for Source Parameter Inversion and Ground Motion Prediction Equations. *J. Geophys. Res. Solid Earth* **123**, 5886–5901 (2018).
37. Atterholt, J., Zhan, Z., Shen, Z. & Li, Z. A unified wavefield-partitioning approach for distributed acoustic sensing. *Geophys. J. Int.* **228**, 1410–1418 (2021).
38. van den Ende, M. *et al.* A Self-Supervised Deep Learning Approach for Blind Denoising and Waveform Coherence Enhancement in Distributed Acoustic Sensing Data. *IEEE Trans. Neural Netw. Learn. Syst.* 1–14 (2021) doi:10.1109/TNNLS.2021.3132832.
39. Trugman, D. T. & Shearer, P. M. Strong Correlation between Stress Drop and Peak Ground Acceleration for Recent M 1–4 Earthquakes in the San Francisco Bay Area. *Bull. Seismol. Soc. Am.* **108**, 929–945 (2018).
40. Trugman, D. T., Page, M. T., Minson, S. E. & Cochran, E. S. Peak Ground Displacement Saturates Exactly When Expected: Implications for Earthquake Early Warning. *J. Geophys. Res. Solid Earth* **124**, 4642–4653 (2019).
41. Oth, A., Miyake, H. & Bindi, D. On the relation of earthquake stress drop and ground motion variability. *J. Geophys. Res. Solid Earth* **122**, 5474–5492 (2017).
42. Kaneko, Y. & Shearer, P. M. Variability of seismic source spectra, estimated stress drop, and radiated energy, derived from cohesive-zone models of symmetrical and asymmetrical circular and elliptical ruptures. *J. Geophys. Res. Solid Earth* **120**, 1053–1079 (2015).
43. Kohler, M. D. *et al.* Earthquake Early Warning ShakeAlert 2.0: Public Rollout. *Seismol. Res. Lett.* **91**, 1763–1775 (2020).

44. Mateeva, A. *et al.* Distributed acoustic sensing for reservoir monitoring with vertical seismic profiling: Distributed acoustic sensing (DAS) for reservoir monitoring with VSP. *Geophys. Prospect.* **62**, 679–692 (2014).
45. Munn, J. D., Coleman, T. I., Parker, B. L., Mondanos, M. J. & Chalari, A. Novel cable coupling technique for improved shallow distributed acoustic sensor VSPs. *J. Appl. Geophys.* **138**, 72–79 (2017).
46. Taner, M. T., Koehler, F. & Sheriff, R. E. Complex seismic trace analysis. *GEOPHYSICS* **44**, 1041–1063 (1979).
47. Brune, J. N. Tectonic stress and the spectra of seismic shear waves from earthquakes. *J. Geophys. Res.* **75**, 4997–5009 (1970).
48. Lior, I. & Ziv, A. The Relation between Ground Acceleration and Earthquake Source Parameters: Theory and Observations. *Bull. Seismol. Soc. Am.* **107**, 1012–1018 (2017).
49. Luco, J. E. On strong ground motion estimates based on models of the radiated spectrum. *Bull. Seismol. Soc. Am.* **75**, 641–649 (1985).
50. Hanks, T. C. b values and $\omega^{-\gamma}$ seismic source models: Implications for tectonic stress variations along active crustal fault zones and the estimation of high-frequency strong ground motion. *J. Geophys. Res.* **84**, 2235 (1979).
51. McGuire, R. K. & Hanks, T. C. RMS accelerations and spectral amplitudes of strong ground motion during the San Fernando, California earthquake. *Bull. Seismol. Soc. Am.* **70**, 1907–1919 (1980).
52. Anderson, J. G. & Hough, S. E. A model for the shape of the fourier amplitude spectrum of acceleration at high frequencies. *Bull. Seismol. Soc. Am.* **74**, 1969–1993 (1984).
53. Eshelby, J. D. The determination of the elastic field of an ellipsoidal inclusion, and related problems. *Proc. R. Soc. Lond. Ser. Math. Phys. Sci.* **241**, 376–396 (1957).
54. Madariaga, R. Dynamics of an expanding circular fault. *Bull. Seismol. Soc. Am.* **66**, 639–666 (1976).

Acknowledgments

This project has received funding from the UCA^{JEDI} Investments in the Future project managed by the National Research Agency (ANR) with the reference number ANR-15-IDEX-01, and

from the Observatoire de la Côte d’Azur. We thank GTD Grupo SA who provided access to the infrastructure, and el Centro Sismologico Nacional staff who helped in the logistics.

Author contributions

IL designed the presented algorithms, performed the analysis and wrote the initial draft. DR, JPA and AS contributed to the discussion, methodology, interpretation and presentation of the results. DR, JPA, AS, SB, RSO, GAVO and JABP took part in performing DAS measurements.

Competing interests statement

The authors declare that they have no conflict of interest.

Data availability statement

Samples of DAS earthquakes are available on <https://osf.io/4bjph/>.